Mesoscopic simulation of slow structural relaxation in fluid mercury near the metal–nonmetal transition

Mesoscopic simulation of slow structural relaxation in fluid mercury near the metal–nonmetal transition

Hikaru Kitamura

Department of Physics, Kyoto University, Sakyo-ku, Kyoto 606-8502, Japan

Abstract

The Langevin diffusion equation approach is proposed for studying the metal–nonmetal (M–NM) transitions in expanded fluid mercury from a mesoscopic and dynamical viewpoint. In this theory, time evolutions of coarse-grained atomic densities are calculated in accordance with the free energy functionals that incorporate changes in the electronic states across the M–NM transitions. Because of the intrinsically discontinuous nature of the M–NM transitions, irregular mixing of high-density metallic domains and low-density nonmetallic domains is predicted in the M–NM transition range. Thermal fluctuations cause local transformation between metallic and nonmetallic domains. The timescale of structural relaxation involving such a local M–NM transition is remarkably slow, which is reflected in the strikingly slow time decay of the dynamical density correlation functions in the M–NM transition range. This result strongly supports the experimental evidence of slow structural relaxation found through anomalous sound wave attenuation. An increase in isothermal compressibilities and a modest enhancement of long-wavelength static structure factors are predicted across the transition. Discontinuous density jumps are smeared out by structural disorder, leading to a continuous M–NM transition in agreement with observations.

1. Introduction

Expanded fluid metals undergo metal–nonmetal (M–NM) transitions and gas–liquid transitions [1]. Elucidation of the electronic and thermodynamic properties and the mechanisms of phase transitions in expanded fluid metals remains one of the basic outstanding issues in condensed-matter physics [1–4]. The optical gap and Knight shift measurements have revealed that M–NM transitions of mercury take place in the density range of 8–10 g cm^{-3} [1, 4]. In this regime, the transition proceeds gradually, without sharp discontinuities in the thermodynamic quantities or transport coefficients such as the electronic conductivities. The

gas–liquid critical point is located at a lower density, $\rho_c = 5.8$ g cm^{-3}, with the critical temperature of $T_c = 1751$ K [1, 4].

Basic mechanisms for the M–NM transitions have been argued from the point of view of electronic-state theories. At low densities, the highest occupied band is the completely filled 6s band, which is separated from the unoccupied 6p band by a finite energy gap; the system thus exhibits semiconducting behaviour. The energy gap decreases as the density increases and eventually overlap of the 6s and 6p bands occurs, where the system turns into a metallic state [1, 4]. Numerical results of the *ab initio* molecular dynamics simulations by Kresse and Hafner [5] support such a simple band overlap transition mechanism, where localization or correlation of electrons does not play a significant role. The non-ideal-plasma theories [6] described the M–NM transition in terms of pressure ionization and predicted a sudden increase of Hg^{2+} ions across metallization.

In addition to such an electronic origin, it is also essential to consider the effect of atomic structural disorder on the M–NM transitions. X-ray diffraction measurements of static structure factors and radial distribution functions [9] have revealed that fluid mercury undergoes *inhomogeneous* expansion, where atomic coordination numbers change appreciably with density while interatomic distances are kept almost constant. The interplay between density inhomogeneities and thermodynamic/transport properties near M–NM transitions have been investigated through theoretical models, such as semiclassical percolation theories [7] and lattice-gas theories [2, 8, 10, 11].

Most of the previous studies mentioned above have focused on the *static* aspect of the M–NM transitions. Recently, there appeared experimental reports by Kohno and Yao [12] on evidence of slow structural relaxation associated with the M–NM transition in fluid mercury. These authors observed anomalous sound attenuation in the M–NM transition range (8–10 g cm^{-3}), which was interpreted as an increase of bulk viscosity due to slow relaxation [13]. By adopting the Debye relaxation formula for the bulk viscosity, these authors evaluated the relaxation time to be approximately 2 ns throughout the M–NM transition range. Because this timescale is considerably larger than the typical timescale of individual atomic motion in liquids (roughly of the order of picoseconds [14]), participation of large-scale atomic motion in slow relaxation is strongly suggested.

Elucidation of the origin of slow structural relaxation is beyond the capability of the *ab initio* microscopic simulations [5], due to limitations on system size and/or computational time. An alternative theoretical tool, which is more suitable for the present purpose, is the Langevin equation approach, in which mesoscopic atomic structures may be described by the appropriate free energy functionals and thermal fluctuations are mimicked by the random Gaussian noise [15–17]. Formulations of simple Langevin diffusion (LD) equations for density fluctuation in liquids have been put forward by Munakata [16] in the context of dynamical density functional theory. So far, the Langevin equation approach has been applied to simple liquids where electrons do not play explicit roles [15, 16]. We expect that the additional inclusion of electronic contributions into the free energy functionals in the LD equations would enable one to treat interesting situations where slow atomic dynamics is interrelated with the electronic transitions, and to gain insights into *dynamical* aspects of the M–NM transitions in liquids.

The principal aim of this paper is to construct a LD approach for simulating mesoscopic atomic dynamics in the M–NM transition range of fluid mercury, and thereby to elucidate the physical origin of the observed slow structural relaxation. Analytic expressions of Helmholtz free energies for homogeneous metallic and nonmetallic phases are needed as an input to the LD equations; they are formulated in sections 2 and 3, respectively. Through comparison of the metallic and nonmetallic free energies, we present naive considerations of the M–NM

transitions in section 4. The LD equation is then formulated in section 5. Numerical simulations based on the LD equation are carried out near M–NM transitions and results on static and dynamical properties are given in section 6. Finally, section 7 is devoted to a summary and discussion.

2. Nonmetallic phase

Fluid mercury in the nonmetallic phase can be regarded as a mixture of neutral Hg atoms, Hg^+ ions and conduction electrons (e^-). Let us write the total atomic density as n and the ionization degree as c_I. The number densities of Hg, Hg^+ and e^-, are then given by $n(1 - c_I)$, nc_I and nc_I, respectively. We assume weak ionization $c_I \ll 1$, which is proven to be valid in the nonmetallic phase; this assumption allows one to treat conduction electrons with classical statistics. Contributions from molecules and clusters are expected [4, 20] but are neglected here for simplicity.

The interaction between Hg atoms may be described by the Lennard-Jones potential, $V_{LJ}(r) = 4\epsilon_{vdW}[(\sigma/r)^{12} - (\sigma/r)^6]$, where the potential parameters have been determined from viscosity measurements in the low-density gas phase [18] as

$$\sigma = 2.898 \text{ Å}, \qquad \epsilon_{vdW}/k_B = 851 \text{ K}. \tag{1}$$

We assume that Hg^+ ions also have the same core diameter, σ.

Conduction electrons produce electric fields and induce electric dipole moments in surrounding Hg atoms. The resultant e^-–Hg interaction plays a crucial role near the gas–liquid critical point [1, 6]; it is an attractive interaction and may be modelled [19] by a potential $V_{pol}(r) = -\alpha e^2/2(r^2 + r_\alpha^2)^2$, where r denotes the interparticle distance and $\alpha = 37a_B^3$ represents the atomic polarizability of a Hg atom [20], with a_B being the Bohr radius. The short-range cut-off parameter r_α has been introduced to avoid unphysical divergence at $r \to 0$.

The Helmholtz free energy in units of Vk_BT/σ^3, with V being the volume of the system and T being the temperature, due to the e^-–Hg interaction may be estimated roughly as

$$\mathcal{F}_{pol} = \frac{4\pi n^2 c_I(1 - c_I)\sigma^3}{k_B T} \int_0^{r_{cut}} dr \, r^2 V_{pol}(r) \simeq -\frac{\epsilon_{pol}}{k_B T}\left(1 - \frac{4}{\pi}\frac{r_\alpha}{r_{cut}}\right)\phi^2 c_I(1 - c_I), \tag{2}$$

where the parameter

$$\epsilon_{pol} \equiv \pi^2 \frac{\alpha}{\sigma^3}\frac{e^2}{r_\alpha} \tag{3}$$

measures the strength of the e^-–Hg interaction, and $\phi \equiv n\sigma^3$. In deriving the last equality in equation (2), we have assumed $r_\alpha \ll r_{cut}$, which is actually satisfied throughout the nonmetallic phase under consideration.

The upper cut-off distance r_{cut} in equation (2) describes the screening length of the e^-–Hg interaction, which means that each conduction electron can attract those atoms that lie within a sphere of radius r_{cut} around it. Noting that there are many conduction electrons in the system, geometrical considerations lead us to an estimation $r_{cut} = \zeta a_e$, where $a_e \equiv (3/4\pi nc_I)^{1/3}$ denotes the average distance between conduction electrons and ζ is an adjustable parameter of the order of unity. Local-field effects arising from many-body dipolar interactions reduce e^-–Hg interactions slightly [19], but they are not considered here for simplicity.

We also remark here that the Hg^+–Hg interaction is a secondary effect compared with the e^-–Hg interaction [1], because the short-range cut-off radius for the former is $\sigma/2$, which is larger than r_α as we shall see later.

In terms of the dimensionless total atomic density $\phi \equiv n\sigma^3$, the total Helmholtz free energy in units of Vk_BT/σ^3 may then be expressed as [20]

$$
\begin{aligned}
\mathcal{F}_{NM}(\phi, c_I) = {}& \phi(1 - c_I)\left\{\ln\left[\left(\frac{\lambda_A}{\sigma}\right)^3 \phi(1 - c_I)\right] - 1\right\} - \phi\ln(1 - \phi) - \frac{4\epsilon_{vdW}}{k_BT}\phi^2(1 - c_I)^2 \\
& + \phi c_I\left\{\ln\left[\left(\frac{\lambda_A}{\sigma}\right)^3 \phi c_I\right] + \ln\left[\left(\frac{\lambda_e}{\sigma}\right)^3 \phi c_I\right] - 2\right\} + \frac{I_{p1}}{k_BT}\phi c_I \\
& - \frac{\epsilon_{pol}}{k_BT}[1 - A(\phi c_I)^{1/3}]\phi^2 c_I(1 - c_I),
\end{aligned} \tag{4}
$$

where $\lambda_A \equiv \sqrt{2\pi\hbar^2/m_A k_B T}$ and $\lambda_e \equiv \sqrt{2\pi\hbar^2/m_e k_B T}$ are thermal de Broglie wavelengths for atoms (ions) and electrons, respectively; $m_A = 3.331 \times 10^{-22}$ g denotes the atomic mass, m_e designates the electron mass and $I_{p1}/k_B = 1.211 \times 10^5$ K is the first ionization energy of an isolated Hg atom [21]. The second ionization energy for the process $Hg^+ \rightarrow Hg^{2+} + e^-$ amounts to $I_{p2}/k_B = 2.177 \times 10^5$ K [21], which is so large that the contributions of Hg^{2+} ions may be neglected [6]. The second term on the right-hand side of equation (4) describes the hard-core repulsion, while the third term refers to the van der Waals attractive interaction among neutral Hg atoms. The final negative term corresponds to the e^-–Hg interaction, with

$$
A = \frac{4}{\pi}\left(\frac{4\pi}{3}\right)^{1/3}\frac{r_\alpha}{\zeta\sigma}. \tag{5}
$$

For given ϕ and T, the degree of ionization c_I is determined through minimization of equation (4), $(\partial\mathcal{F}/\partial c_I)_{\phi,T} = 0$, which yields

$$
c_I = \sqrt{2\left(\frac{\sigma}{\lambda_e}\right)^3 \frac{1}{\phi}}\exp\left(-\frac{\Delta G}{2k_B T}\right), \tag{6}
$$

with

$$
\Delta G = I_{p1} - \epsilon_{pol}\phi(1 - 2c_I) + 8\epsilon_{vdW}\phi(1 - c_I) + \epsilon_{pol}A(\phi c_I)^{1/3}\phi\left(\frac{4}{3} - \frac{7}{3}c_I\right). \tag{7}
$$

Equation (6) takes the form of the law of mass action, with equation (7) representing an effective energy of promoting one electron from the valence band to the conduction band. Since ΔG depends on c_I, equation (6) should be solved numerically in a self-consistent manner.

The pressure in units of $k_B T/\sigma^3$, which we write as $\mathcal{P}_{NM}$, can be obtained through equations (4) and (6) as $\mathcal{P}_{NM} = \phi(\partial\mathcal{F}_{NM}/\partial\phi)_{c_I,T} - \mathcal{F}_{NM}$, leading to

$$
\mathcal{P}_{NM}(\phi, c_I) = \frac{\phi}{1 - \phi} - \frac{4\epsilon_{vdW}}{k_BT}\phi^2(1 - c_I)^2 + \phi c_I - \frac{\epsilon_{pol}}{k_BT}\left[1 - \frac{4}{3}A(\phi c_I)^{1/3}\right]\phi^2 c_I(1 - c_I). \tag{8}
$$

Formula (8) indicates that both the van der Waals and e^-–Hg interaction terms make *negative* contributions to the pressure, causing gas–liquid transitions. The critical density ϕ_c and critical temperature T_c are determined through solutions to the equation

$$
\left(\frac{\partial\mathcal{P}_{NM}}{\partial\phi}\right)_T = \left(\frac{\partial^2\mathcal{P}_{NM}}{\partial\phi^2}\right)_T = 0, \tag{9}
$$

where the derivatives should be taken under the ionization equilibrium condition, $(\partial\mathcal{F}_{NM}/\partial c_I)_{\phi,T} = 0$.

The predictions of ϕ_c and T_c depend on the two adjustable parameters, r_α and ζ. We optimize these parameters so that we can reproduce the experimental critical point, $\rho_c = 5.8$ g cm^{-3} ($\phi_c = 0.424$) and $T_c = 1750$ K. We thus obtain

$$
r_\alpha = 0.942 \text{ Å}, \qquad \zeta = 0.336. \tag{10}
$$
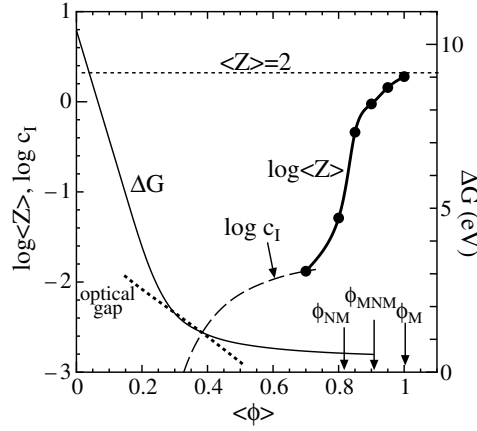
Figure 1. The ionization degree at $T = T_c = 1750$ K as a function of density. Dots and the thick full curve refer to the simulation results of $\langle Z \rangle$, while the broken curve refers to the prediction on c_I by equation (6). Plots of ΔG (thin full curve) and the experimentally measured optical gap [4] (dotted curve) are also presented in units of eV.

The critical pressure turns out to be $P_c = 2.71$ kbar, which is somewhat larger than the experimental value of 1.67 kbar. The fact that $r_\alpha < \sigma/2$ indicates that conduction electrons can penetrate into the core of an atom. The above estimation leads to $A = 1.99$ and $\epsilon_{pol}/k_B = 3.93 \times 10^5$ K. A large value of ϵ_{pol} is especially notable when it is compared with thermal energy and van der Waals energy. Substantial enhancement of the critical temperature is brought about by the e^-–Hg interaction [6].

In figure 1, we plot ΔG and c_I at $T = T_c = 1750$ K as functions of ϕ. The ionization degree at the critical point is $c_I = 4.3 \times 10^{-3}$. At low densities, ΔG decreases linearly with ϕ, because $c_I \ll 1$ and $\Delta G \approx I_{p1} - \epsilon_{pol}\phi$ from equation (7); ionization proceeds rapidly with increasing ϕ. As ϕ becomes comparable to ϕ_c, the density dependence of ΔG becomes weaker, because the screening factor of the e^-–Hg interaction, which is expressed as $A(\phi c_I)^{1/3}$ in equation (7), begins to play a role. We find that the overall behaviour of ΔG is in reasonable agreement with the more detailed calculation by Nagel *et al* [6] and also with the measured optical gap near ϕ_c [4].

3. Metallic phase

When the density becomes so high that valence and conduction bands overlap, the system enters the metallic phase consisting of doubly charged ions (Hg^{2+}) and degenerate conduction electrons (e^-). Let the number density of ions be n. The electron density is then $n_e = Zn$; Z is the ionic valence, which we set as $Z = 2$ hereafter.

Total free energies of fluid metallic mercury may be decomposed into contributions from the ionic subsystem, electronic subsystem and electron–ion interaction [22, 23], that is:

$$\mathcal{F}_M(\phi) = \phi\left\{\ln\left[\left(\frac{\lambda_A}{\sigma}\right)^3 \phi\right] - 1\right\} - \phi\ln\left[1 - \left(\frac{\sigma_I}{\sigma}\right)^3 \phi\right] + Z\phi\left(f_e^{id} + f_{ee}\right) + \phi\frac{I_{p1} + I_{p2}}{k_B T}$$
$$+ \phi[u_{ex}^{OCP}(\Gamma) - s_{ex}^{OCP}(\Gamma_{eff}) + u_{BS} + u_0]. \tag{11}$$

Here, $\phi \equiv n\sigma^3$ is the dimensionless atomic density defined in section 2; σ_I represents the core diameter of a Hg^{2+} ion. Since the radial distribution function in the metallic regime virtually

vanishes at $r < 2.0$ Å [5, 9], we may set $\sigma_I = 2.0$ Å. We have confirmed that the total free energy is not so sensitive to the choice of σ_I.

To describe the electronic system, we introduce a dimensionless density parameter and Coulomb coupling parameter according to [24]:

$$r_s = \frac{a_e}{\hbar^2/m_e e^2}, \qquad \Gamma_e = \frac{e^2}{a_e k_B T}, \tag{12}$$

where $a_e = (3/4\pi n_e)^{1/3}$ is the Wigner–Seitz radius and m_e is the electron mass.

The function f_e^{id} refers to the free energy per particle of the ideal-gas electrons in units of $k_B T$; it is expressed as $f_e^{id} = 3E_F/5k_B T$, with the Fermi energy $E_F = \hbar^2(3\pi^2 n_e)^{2/3}/2m_e$. The condition $E_F \gg k_B T$ is satisfied throughout the density regime under consideration, so that finite-temperature effects for the electrons can be neglected.

The exchange–correlation free energy of the electron liquid can be written as [24]

$$f_{ee} = \left[-\frac{3}{4}\left(\frac{3}{2\pi}\right)^{2/3} + \frac{r_s}{2} E_c(r_s) \right] \Gamma_e, \tag{13}$$

where the correlation energy $E_c(r_s)$ has been expressed in a parametrized form by Vosko *et al* [25], on the basis of the Green function Monte Carlo data by Ceperley and Alder [26].

The Madelung energy of the ions immersed in a uniform background of negative charges may be evaluated by the excess internal energy formula of the classical one-component plasma (OCP). We use the analytic expression based on the Monte Carlo results by Ogata and Ichimaru [24]:

$$u_{ex}^{OCP}(\Gamma) = -0.898\,004\Gamma + 0.967\,86\Gamma^{1/4} + 0.220\,703\Gamma^{-1/4} - 0.860\,97, \tag{14}$$

with the Coulomb coupling parameter for a classical ion OCP being given by $\Gamma = Z^{5/3}\Gamma_e$. Formula (14) is valid in the strong coupling regime, $1 \leqslant \Gamma < 180$.

We formulate electron–ion interaction free energies by following the conventional pseudopotential perturbation theory in the nearly-free electron approximation [22, 23]. For the electron–ion interaction, we adopt Shaw's model potential [22, 27]:

$$V^p(r) = \begin{cases} -Ze^2/R_M, & \text{for } r < R_M, \\ -Ze^2/r, & \text{for } r \geqslant R_M, \end{cases} \tag{15}$$

where R_M is an adjustable parameter, to be determined below. The contributions of the electron–ion interaction to the free energy may be divided into the so-called Hartree energy u_0 and the band structure energy u_{BS} [22, 23]. The Hartree energy is independent of the ionic structure and is evaluated as

$$u_0 = \frac{1}{2}\left(\frac{R_M}{a_e}\right)^2 Z\Gamma_e. \tag{16}$$

The quantities u_{BS} and $s_{ex}^{OCP}(\Gamma)$ depend explicitly on the ionic structure. The static structure factors of the ions are usually approximated by those of a suitable reference system, either a hard-sphere or OCP fluid, with the variational parameters being determined through minimization of the total free energy [23, 29]. For the purpose of constructing the analytic free energy formula, however, we considerably simplify this procedure and employ an approximate analytic expression for the band structure energy as

$$u_{BS} = -\frac{Z^{1/3}a_e}{4R_M^2 k_{IS}}\Gamma\left[\frac{1}{k_{IS}D_s + 1} - \frac{k_{IS}D_s\exp(-2R_M/D_s) - \exp(-2k_{IS}R_M)}{k_{IS}^2 D_s^2 - 1} \right]. \tag{17}$$

Here, $k_{IS} = 1.8/(Z^{1/3}a_e)$ is a parameter related to the ionic structure factor; D_s is the short-range screening distance of the electrons which is related to the dielectric response of the

electrons against ions. A simple fitting formula for D_s is available for degenerate electron liquids [24, 28], which is

$$D_s = \frac{a_e}{1.239 r_s^{0.435}}. \tag{18}$$

The derivation of equation (17) is explained in the appendix.

The excess entropy of the ionic system may likewise be evaluated on the basis of the Monte Carlo data for OCP [24], which may be written as

$$s_{ex}^{OCP}(\Gamma) = -2.902\,68\Gamma^{1/4} + 1.103\,515\Gamma^{-1/4} + 0.860\,97\ln\Gamma + 1.665\,95, \tag{19}$$

In applying this formula to equation (12), reduction of interionic Coulomb repulsion due to electron screening is taken into account through introducing the effective Coulomb-coupling parameter Γ_{eff} [24, 28]:

$$\Gamma_{eff} = \Gamma \exp\left(-\kappa \frac{Z^{1/3} a_e}{D_s}\right), \tag{20}$$

where κ is an adjustable parameter of the order of unity.

Three adjustable parameters R_M and κ are determined through comparison with existing experimental data at atmospheric pressure [22]. We thus adopt

$$R_M = 1.14\,\text{Å}, \qquad \kappa = 0.7. \tag{21}$$

With the use of these parameter values, the cohesive energy (relative to Hg gas) at 273 K is calculated as 0.0530 Ryd/atom, which is in reasonable agreement with the experimental value, 0.04 Ryd/atom. The calculated equilibrium density at 273 K is 13.6 g cm^{-3}, which agrees excellently with the experimental value. The entropy per atom in units of k_B amounts to 5.23 at melting temperature (234 K), while the corresponding experimental value is 8.0.

We list typical values of the plasma parameters defined above. At $\phi = 0.9$ and $T = 1750$ K, which is in the M–NM transition range, we have $r_s = 2.8$, $k_B T/E_F = 0.023$, $\Gamma = 205$ and $\Gamma_{eff} = 37$. Smallness of $k_B T/E_F$ validates our use of a zero-temperature equation of state for the electrons. The difference between Γ_{eff} and Γ manifests the reduction of interionic Coulomb repulsion due to electron screening.

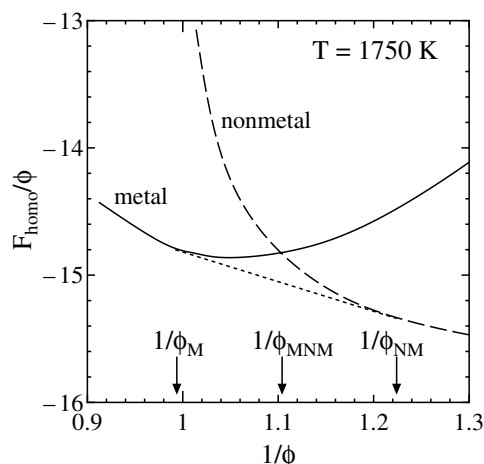## 4. Metal–nonmetal transition

A salient feature concerning the M–NM transition is the possible occurrence of a first-order phase transition [2]. Figure 2 illustrates the free energy per atom for the metallic phase and that for the nonmetallic phase at $T = 1750$ K plotted against the dimensionless atomic volume. One finds the M–NM transition density ϕ_{MNM} at which the crossover takes place from the nonmetallic branch to metallic branch, i.e. $\mathcal{F}_{NM}(\phi_{MNM}) = \mathcal{F}_M(\phi_{MNM})$. A kink appears in the free energy curve due to a sudden change in the nature of the cohesive force at ϕ_{MNM}. One can then construct a common tangent to the free energy curve with two contact points, ϕ_{NM} and ϕ_M. This is a *first-order phase transition*, characterized by a discontinuous change in ϕ from ϕ_{NM} to ϕ_M [2].

It should be noted, however, that the experimentally observed equation of state and electrical conductivities change continuously with density and show no clear evidence of a discontinuous phase transition [1, 3]. As we shall see in the next section, structural disorder arising from thermal fluctuations smears out the discontinuous jump of density and makes the M–NM transitions continuous.

The contours of ϕ_{NM}, ϕ_M and ϕ_{MNM} so obtained are exhibited in figure 3 together with the gas–liquid coexistence curve. The region $\phi_{NM} \leqslant \phi \leqslant \phi_M$ designates the M–NM transition

Figure 2. Comparison of the free energies, $\mathcal{F}_{NM}(\phi)/\phi$ (broken curve) and $\mathcal{F}_M(\phi)/\phi$ (full curve) at $T = 1750$ K. The common tangent to these free energy curves is depicted by the dotted line.
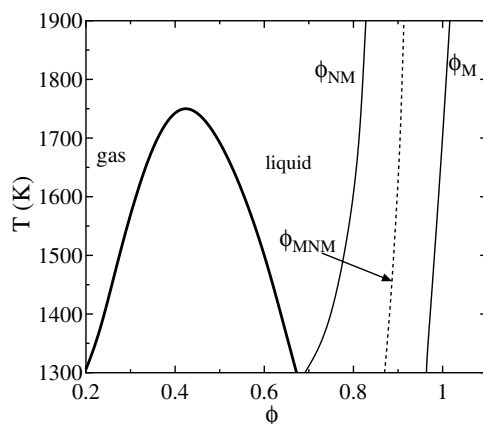
Figure 3. Plot of the M–NM transition line (dotted curve), metallic and nonmetallic phase boundaries (full curves) and the gas–liquid coexistence curve (thick full curve) obtained through equations (4) and (11).

range. It is found that the temperature dependence of ϕ_{MNM} is relatively weak and the M–NM transition is controlled mainly by the atomic density.

The M–NM transition density is determined through a delicate balance between the metallic and nonmetallic free energies, which makes it difficult to determine the value of ϕ_{MNM} accurately. Indeed, the present theory predicts the M–NM transition in the density range of 11.2–13.7 g cm^{-3}, while the experimentally observed transition range is 8–10 g cm^{-3} [4]. It is likely that the origin of such disagreement is the breakdown of the nearly-free electron approximation in the metallic free energy. Since metallic mercury is divalent, the electron–ion interaction is stronger compared with monovalent alkali metals. Consideration of strong electron–ion coupling [28] would lead to a reduction of the electron screening length D_s and thus to stabilizing the metallic phase at lower densities. Such an improvement of the equations of state is not pursued in the present paper, however.

5. Langevin diffusion equation

When the state of a fluid is in the M–NM transition range, there is a possibility that thermal fluctuations spontaneously generate high-density metallic regions and low-density nonmetallic regions in the system. Let $\phi(\mathbf{r}, t)$ be the dimensionless local atomic density at position $\mathbf{r}$ and time t. The hydrodynamic approach is considered here, so that $\phi(\mathbf{r}, t)$ should be interpreted as a quantity obtained by averaging microscopic local atomic density over a volume $(\Delta r)^3$ that is macroscopically small but large enough to contain a number of atoms inside it [14]. Time evolutions of $\phi(\mathbf{r}, t)$ may then be calculated through the LD equation [16]:

$$\frac{\partial \phi(\mathbf{r}, t)}{\partial t} = \nabla \cdot \left\{ D\phi(\mathbf{r}, t)\nabla \frac{\delta(\beta\sigma^3 F)}{\delta\phi(\mathbf{r}, t)} \right\} - \nabla \cdot \mathbf{j}_{\mathrm{R}}(\mathbf{r}, t). \tag{23}$$

Here, the parameter D refers to the diffusion constant, whose density–temperature dependence is neglected for simplicity; $\beta \equiv 1/k_{\mathrm{B}}T$ refers to the inverse temperature.

In equation (23), $F[\phi]$ stands for the Helmholtz free energy functional. We adopt the coarse-grained functional form based on the square-gradient approximation [33] as

$$\beta\sigma^3 F[\phi] = \int \mathrm{d}\mathbf{r} \, \mathcal{F}[\phi(\mathbf{r}, t)] = \int \mathrm{d}\mathbf{r} \left[\mathcal{F}_{\mathrm{homo}}[\phi(\mathbf{r}, t)] + \frac{C_{\mathrm{grad}}}{2} |\nabla\phi(\mathbf{r}, t)|^2 \right]. \tag{24}$$

The functional derivative in equation (23) can then be evaluated as

$$\frac{\delta(\beta\sigma^3 F)}{\delta\phi(\mathbf{r}, t)} = \frac{\partial \mathcal{F}_{\mathrm{homo}}(\phi(\mathbf{r}, t))}{\partial \phi(\mathbf{r}, t)} - C_{\mathrm{grad}}\nabla^2\phi(\mathbf{r}, t). \tag{25}$$

The function $\mathcal{F}_{\mathrm{homo}}(\phi)$ refers to the free energy density of the homogeneous phase. As we have seen in the previous section, it is expressed as

$$\mathcal{F}_{\mathrm{homo}}(\phi) = \begin{cases} \mathcal{F}_{\mathrm{NM}}(\phi), & \text{for } \phi < \phi_{\mathrm{MNM}}, \\ \mathcal{F}_{\mathrm{M}}(\phi), & \text{for } \phi \geqslant \phi_{\mathrm{MNM}}, \end{cases} \tag{26}$$

in conjunction with equations (4) and (11). The electronic transitions are described by equation (26), which in turn affects atomic density fluctuations through equation (23).

The coefficient of the gradient term, C_{grad}, is related to the long-wavelength behaviour of the Fourier-transformed direct correlation function $c(k)$ [14, 33, 34], that is:

$$C_{\mathrm{grad}} = -\frac{1}{2\sigma^3} \frac{\mathrm{d}^2 c(k = 0)}{\mathrm{d}k^2} \equiv -\frac{1}{2\sigma^3} c''(0). \tag{27a}$$

It has been known that $c(k)$ is related to the static structural factor $S(k)$ of the ions [14]. Experimental data on $S(k)$, though not available for the very small k regime, exhibit a minimum at about $1 \, \text{Å}^{-1}$ in the nonmetallic phase, which is not clearly seen in the metallic phase [35]. This suggests that $c''(0) > 0$ in the dense metallic regime and $c''(0) < 0$ in the nonmetallic phase close to the gas–liquid critical point [36]. Therefore, we expect that $c''(0)$, and hence C_{grad}, may be close to zero in the intermediate density range near the M–NM transitions. This trend has actually been predicted by theoretical calculations for liquid alkali metals [34]. Near the gas–liquid critical point where $c''(0) < 0$, it is convenient to rewrite equation (27a) in the form

$$C_{\mathrm{grad}} = \frac{\xi^2}{\phi} \left(\frac{\partial \mathcal{P}_{\mathrm{homo}}}{\partial \phi} \right)_T, \tag{27b}$$

where ξ denotes the correlation length [31]. With the aid of the experimental data on ξ [30] and theoretical calculations of $(\partial \mathcal{P}_{\mathrm{homo}}/\partial\phi)_T$ with equation (8), we can estimate $C_{\mathrm{grad}}/\sigma^2 \approx 11$ near the gas–liquid critical point. Therefore, we may at least infer that $C_{\mathrm{grad}}/\sigma^2 < 11$ in the

M–NM transition range. Since the accurate density–temperature dependence of C_{grad} is not known for mercury, we simply study the two cases, $C_{grad}/\sigma^2 = 9.0$ and 1.0.

The random noise current $\mathbf{j}_R(\mathbf{r}, t)$ describes the effect of thermal fluctuation. It should satisfy the fluctuation-dissipation theorem [16]:

$$\langle j_{Ri}(\mathbf{r}, t) j_{Rj}(\mathbf{r}', t') \rangle = 2D\phi(\mathbf{r}, t)\sigma^3 \delta_{ij}\delta(\mathbf{r} - \mathbf{r}')\delta(t - t') \qquad (i, j = x, y, z), \qquad (28)$$

where $\langle \cdots \rangle$ denotes the statistical average. It can then be proven [16] that the LD equation (23) samples density fluctuations with the Boltzmann weight $\exp(-\beta F[\phi])$.

The derivation of equation (23) involves several assumptions: first, it has been assumed that ϕ is the only variable that changes slowly in time; the time dependence of other quantities, such as the velocity field, has been neglected [16]. Such an assumption may be validated in the present study, because we are concerned with slow density relaxation. Second, as usual, we have assumed that the electronic states are determined instantaneously for a given atomic configuration (*adiabatic approximation*). Finally, local charge neutrality and local thermodynamic equilibrium are assumed.

Equation (23) can be rewritten in a dimensionless form in such a way that the length and time are measured in units of σ and σ^2/D, respectively [16]. Numerical simulations based on equation (23) have then been performed in a two-dimensional space, because full three-dimensional simulations may cost too much computational time to explore the dependences of the numerical results on various input parameters. It should be stressed here that we use the free energy functionals formulated for the usual three-dimensional fluids. We shall discuss later in section 7 how the final results may be modified in the case of three-dimensional simulations.

Numerical integrations of equation (23) have been carried out using the Euler algorithm with the time step $\Delta t = 0.02\sigma^2/D$, for a square supercell of length L. Periodic boundary conditions have been imposed. The supercell has been divided into $N \times N$ pieces of cells, each having a linear dimension Δr; we adopt $N = 128$ for all simulation runs. In light of the two-dimensional counterpart to expression (28), the noise current is generated for each cell and each time step in accordance with

$$j_{Ri}(\mathbf{r}, t) = \sqrt{\frac{2\phi(\mathbf{r}, t)D}{(\Delta t)(\Delta r/\sigma)^2}} p(\mathbf{r}, t), \qquad (i, j = x, y), \qquad (29)$$

where $p(\mathbf{r}, t)$ represents the normal (Gaussian) deviate with zero mean and unit variance.

The appropriate choice of cell size Δr should be mentioned [37]. Apparently, Δr should be sufficiently large so that the use of the bulk free energy for each cell can be justified. When Δr is set too large, however, the possibilities of a simultaneous coexistence of metallic and nonmetallic phases in a single cell may be overlooked. It may be reasonable to set Δr close to the possible minimum size of a metallic domain. In this regard, we notice the theoretical study by Pastor and Bennemann [32], showing that a mercury cluster exhibits electronic states characteristic of a bulk metal when the number of constituent atoms exceeds approximately 80. The linear dimension of such a cluster may be estimated roughly as $80^{1/3}\sigma = 4.3\sigma$ by assuming a nearest-neighbour distance of σ. In this way, we adopt $\Delta r = 4\sigma$ in most of the simulation runs; the dependence of the final results on the choice of Δr will be argued later in section 6.3.

Each simulation run has been started with an initial condition with a homogeneous density distribution, i.e. $\phi(\mathbf{r}, t = 0) = \langle\phi\rangle$. Density inhomogeneity is then generated by the random force, equation (29). Total simulation time for each run is 300–4500 in units of σ^2/D after thermal equilibration has been achieved.
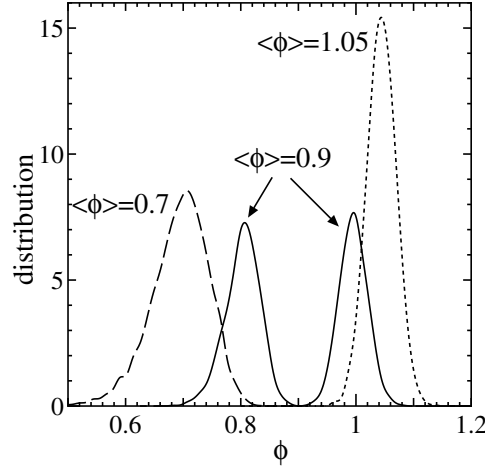
Figure 4. Snapshot of the histogram of ϕ at $T = 1750$ K for three different average densities: $\langle \phi \rangle = 0.7$ (broken curve), 0.9 (full curve) and 1.05 (dotted curve).

6. Simulation results

6.1. Static properties

Figure 4 illustrates the snapshot of a histogram of local atomic density at $T = 1750$ K, calculated for three different mean densities $\langle \phi \rangle$. At the lowest density $\langle \phi \rangle = 0.7$, corresponding to the pure nonmetallic phase, the histogram exhibits a trivial single-peak structure, indicating density fluctuation around the mean density; the distribution is confined within the nonmetallic phase, $\phi < \phi_{MNM}$. A similar behaviour is observed at the highest density $\langle \phi \rangle = 1.05$, corresponding to the pure metallic phase. At an intermediate density $\langle \phi \rangle = 0.9$, close to the M–NM transition density $\phi_{MNM} = 0.907$, we observe a two-peak structure in contrast to the former two cases. One of the peaks is located at a density in the metallic regime ($\phi > \phi_{MNM}$), while the position of the other peak is contained in the nonmetallic regime ($\phi < \phi_{MNM}$). This indicates the coexistence of metallic and nonmetallic domains in the system. Irregular mixing of the two types of domains is clearly demonstrated in the snapshot of spatial patterns shown in figure 5.

As metallization proceeds, the high-density peak grows and the low-density peak diminishes; the relative fraction of the metallic component increases with $\langle \phi \rangle$, leading to a continuous increase of the ionization degree. We plot in figure 1 the average ionization degree, $\langle Z \rangle$, obtained by taking spatial and time averages of the local ionization degree:

$$Z(\mathbf{r}, t) \equiv \frac{n_e(\mathbf{r}, t)}{n(\mathbf{r}, t)} = \begin{cases} c_I(\mathbf{r}, t), & \text{for } \phi(\mathbf{r}, t) < \phi_{MNM}, \\ 2, & \text{for } \phi(\mathbf{r}, t) \geqslant \phi_{MNM}. \end{cases} \tag{30}$$

A gradual increase of $\langle Z \rangle$ can be found in the M–NM transition range, $\phi_{NM} \leqslant \langle \phi \rangle \leqslant \phi_M$. At lower densities $\langle \phi \rangle < \phi_{NM}$, the metallic component is negligible and $\langle Z \rangle$ asymptotically approaches c_I obtained from equation (6).

To see how such inhomogeneous atomic structures in the M–NM transitions may be reflected in static physical quantities, we calculate the static structure factor, which may be defined in the two-dimensional case as

$$S(k) = \frac{1}{(L\sigma)^2} \frac{\langle |\delta\phi(\mathbf{k}, t)|^2 \rangle}{\langle \phi \rangle}, \tag{31}$$
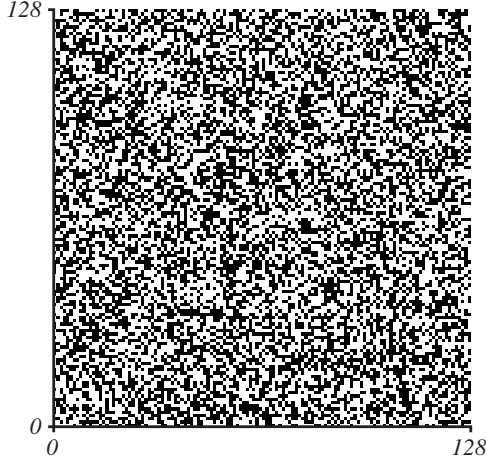
Figure 5. Snapshot of a spatial pattern for $\langle\phi\rangle = 0.9$ and $T = 1750$ K. Metallic domains are plotted in black. The linear dimension of the system is $L = N\Delta r = 1.48 \times 10^3$ Å.

where

$$\delta\phi(\mathbf{k}, t) = \int_{L^2} \mathrm{d}\mathbf{r} \, [\phi(\mathbf{r}, t) - \langle\phi\rangle] \exp(-\mathrm{i}\mathbf{k} \cdot \mathbf{r}). \tag{32}$$

In the density regime far from the M–NM transitions, the magnitude of $\phi - \langle\phi\rangle$ may always be small, as figure 4 indicates. One can then expand $\mathcal{F}_{\mathrm{homo}}(\phi)$ in equation (24) with respect to $\phi - \langle\phi\rangle$ to yield

$$\beta\sigma^3\mathcal{F}[\phi] \simeq \beta\sigma^3\mathcal{F}[\langle\phi\rangle] + \int \mathrm{d}\mathbf{r} \left\{ \frac{1}{2\langle\phi\rangle} \left(\frac{\partial\mathcal{P}_{\mathrm{homo}}(\langle\phi\rangle)}{\partial\phi} \right)_T [\phi(\mathbf{r}, t) - \langle\phi\rangle]^2 \right.$$
$$\left. + \frac{C_{\mathrm{grad}}}{2} |\nabla\phi(\mathbf{r}, t)|^2 \right\}. \tag{33}$$

Then, equation (23) is reduced to the form

$$\frac{\partial\delta\phi(\mathbf{k}, t)}{\partial t} \simeq -\frac{D}{L^2} \sum_{\mathbf{q}} \delta\phi(\mathbf{k} - \mathbf{q}, t) \left[\frac{1}{\langle\phi\rangle} \left(\frac{\partial\mathcal{P}_{\mathrm{homo}}(\langle\phi\rangle)}{\partial\phi} \right)_T + C_{\mathrm{grad}}q^2 \right] \delta\phi(\mathbf{q}, t)\mathbf{q} \cdot \mathbf{k}$$
$$- D\langle\phi\rangle k^2 \left[\frac{1}{\langle\phi\rangle} \left(\frac{\partial\mathcal{P}_{\mathrm{homo}}(\langle\phi\rangle)}{\partial\phi} \right)_T + C_{\mathrm{grad}}k^2 \right] \delta\phi(\mathbf{k}, t) + \theta(\mathbf{k}, t), \tag{34}$$

with

$$\theta(\mathbf{k}, t) = -\mathrm{i}\mathbf{k} \cdot \int_{L^2} \mathrm{d}\mathbf{r} \, \mathbf{j}_{\mathrm{R}}(\mathbf{r}, t) \exp(-\mathrm{i}\mathbf{k} \cdot \mathbf{r}). \tag{35}$$

When we neglect the first (nonlinear) term on the right-hand side of equation (34), which is proportional to $\delta\phi^2$, the steady-state solution to equation (34) can easily be obtained. The static structure factor in such a linearized approximation is thus expressed as

$$S(k) = \frac{1}{(\partial\mathcal{P}_{\mathrm{homo}}(\langle\phi\rangle)/\partial\phi)_T + C_{\mathrm{grad}}\langle\phi\rangle k^2} \xrightarrow{k\to 0} \left(\frac{\partial\mathcal{P}_{\mathrm{homo}}(\langle\phi\rangle)}{\partial\phi} \right)_T^{-1}. \tag{36}$$

One thus finds that, when the linearized approximation is valid, $S(0)$ is simply given by the isothermal compressibility of the *homogeneous* phase evaluated at $\phi = \langle\phi\rangle$, which can be obtained directly through equation (4) or (11).

Figures 6(a) and (b) show the simulation results of $S(k)$ for three different densities, corresponding to those in figure 4. In the pure metallic and nonmetallic phases, the values of $S(k)$ are relatively small over the entire k regime. The extrapolation of the simulation
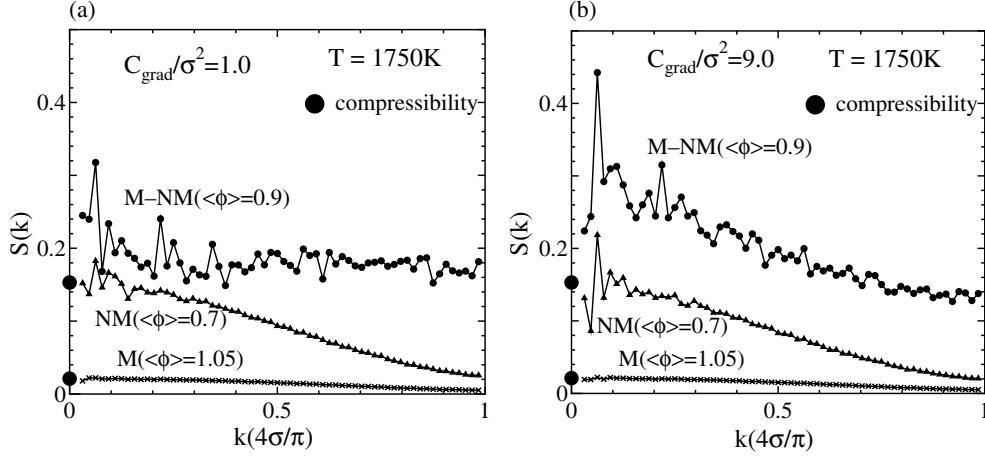
Figure 6. Static structure factors for $T = 1750$ K and $\langle\phi\rangle = 0.7$ (triangles), 0.9 (circles) and 1.05 (crosses), calculated with (a) $C_{\mathrm{grad}}/\sigma^2 = 1.0$ and (b) $C_{\mathrm{grad}}/\sigma^2 = 9.0$. Upper and lower dots at $k = 0$ depict the values of $S(0)$ due to equation (36) for $\langle\phi\rangle = 0.7$ and 1.05, respectively.

data to $k \to 0$ agrees with the compressibility of the corresponding homogeneous phase, as equation (36) indicates. In the case of $\langle\phi\rangle = 0.9$, which corresponds to the M–NM transition range, modest enhancement of $S(k)$ can be observed. It remains to be seen whether such an enhancement can be detected experimentally: the maximum wavenumber for $S(k)$ achieved in this theory is $0.27\,\text{Å}^{-1}$, which is still smaller than the observable low-k limit ($\approx 0.7\,\text{Å}^{-1}$) [35] in the x-ray diffraction measurements. Since separation into metallic and nonmetallic domains occurs, deviations of local density from $\langle\phi\rangle$ are fairly large, so that the linearized solution (equation (36)) is no longer valid in the M–NM transition range.

In the case with $C_{\mathrm{grad}}/\sigma^2 = 9.0$, enhancement of $S(k)$ in the small-k regime turns out to be more pronounced compared to the case with $C_{\mathrm{grad}}/\sigma^2 = 1.0$. When C_{grad} is large, the appearance of the M–NM interface is energetically unfavourable; as a consequence, the size of each domain tends to be large.

By taking spatial and time averages of the local free energy densities, we evaluate the total free energy density of the system according to the relation [37]:

$$\langle\mathcal{F}\rangle = -\left(\frac{\sigma}{L}\right)^2 \ln\left\{\sum_{\{\phi\}} \exp\left[-\frac{1}{\sigma^2}\int_{L^2} d\mathbf{r}\,\mathcal{F}[\phi]\right]\right\}. \tag{37}$$

The pressure (in units of $k_{\mathrm{B}}T/\sigma^3$) can then be computed in accordance with $\mathcal{P} = \langle\phi\rangle(\partial\langle\mathcal{F}\rangle/\partial\langle\phi\rangle)_T - \langle\mathcal{F}\rangle$. The pressure–density relations so obtained are plotted in figure 7. The simulation result with $C_{\mathrm{grad}}/\sigma^2 = 1.0$ shows a continuous increase of pressure as a function of $\langle\phi\rangle$ throughout the M–NM transition range, which is compatible with experimental observations of gradual M–NM transitions [3]. The corresponding simulation result with $C_{\mathrm{grad}}/\sigma^2 = 9.0$ exhibits a regime of negative compressibility, which signals the occurrence of a discontinuous, first-order M–NM transition. When the gradient free energy does not play an important role, the metallic and nonmetallic domains are mixed in an irregular manner and the intrinsically discontinuous nature of the M–NM transitions may thus be smeared out.

Even in the case $C_{\mathrm{grad}}/\sigma^2 = 1.0$, a significant increase of the isothermal compressibility can still be seen in the M–NM transition range. As we observe in figure 6(b), this does not lead to a divergent increase of $S(0)$, because the simple relation between the compressibility and
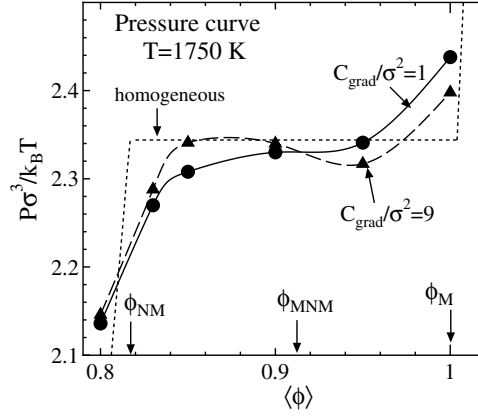
Figure 7. Pressure–density relations at $T = 1750$ K. Simulation results with $C_{grad}/\sigma^2 = 1.0$ and 9.0 are shown by circles and triangles, respectively. The full and broken curves are shown as guides to the eyes. The dotted curve depicts the pressure curve corresponding to the sharp first-order phase transition predicted by the equations of state for the homogeneous phases.

structure factor (equation (36)) no longer applies to an inhomogeneous two-phase state due to the breakdown of the linearized approximation. As we see in figure 5, local densities vary from cell to cell in an irregular way and long-wavelength density fluctuations such as those near gas–liquid criticality cannot be observed.

6.2. Dynamic properties

When external pressure, such as the sound pressure, is suddenly applied to the system, the system is brought to a transient non-equilibrium state, which subsequently undergoes relaxation to a new equilibrium state via structural rearrangement. The dynamical characteristics of such a structural relaxation may be analysed through the decay of the time-dependent density correlation function [15, 16]:

$$C(k, t) = \frac{\langle \delta\phi(\mathbf{k}, t)\delta\phi(-\mathbf{k}, 0)\rangle}{\langle \delta\phi(\mathbf{k}, 0)\delta\phi(-\mathbf{k}, 0)\rangle}. \tag{38}$$

When the amplitude of the density fluctuation is small enough for the linearized approximation to be applicable, $C(k, t)$ can be obtained from equation (34), which shows a simple exponential decay:

$$C(k, t) \simeq \exp\left\{ -\left[\left(\frac{\partial \mathcal{P}_{homo}(\langle\phi\rangle)}{\partial \phi} \right)_T + C_{grad}\langle\phi\rangle k^2 \right] Dk^2 t \right\}. \tag{39}$$

Time evolutions of $C(k, t)$ obtained by the simulation are illustrated in figure 8 for three different densities in the case of $k\sigma = 0.245$. In the nonmetallic ($\langle\phi\rangle = 0.7$) and metallic ($\langle\phi\rangle = 1.05$) phases, $C(k, t)$ decays rapidly, with a timescale comparable to the microscopic diffusion time, σ^2/D; the simulation results are excellently reproduced by the linearized approximation, equation (39). On the other hand, significantly slow relaxation of $C(k, t)$ can be seen in the M–NM transition range ($\langle\phi\rangle = 0.9$); moreover, relaxation of $C(k, t)$ proceeds in two steps, namely a fast relaxation in the early stage ($t < 2\sigma^2/D$) followed by a slow relaxation in the later stage ($t > 2\sigma^2/D$).

Since density fluctuation itself is prevalent in any fluid, ϕ does not serve as a suitable order parameter characterizing the M–NM transition. A relevant order parameter which is directly
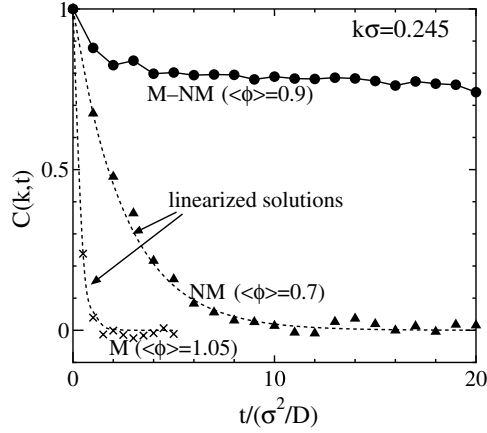
Figure 8. Relaxations of $C(k, t)$ for $k\sigma = 0.245$ and $T = 1750$ K, where $C_{\text{grad}}/\sigma^2 = 1.0$ is adopted. Triangles and crosses represent the simulation results for $\langle\phi\rangle = 0.7$ and 1.05, respectively; the dotted curves are the corresponding linearized solutions, equation (39). The simulation result for $\langle\phi\rangle = 0.9$ is shown by circles and the full curve is for a guide to the eyes.
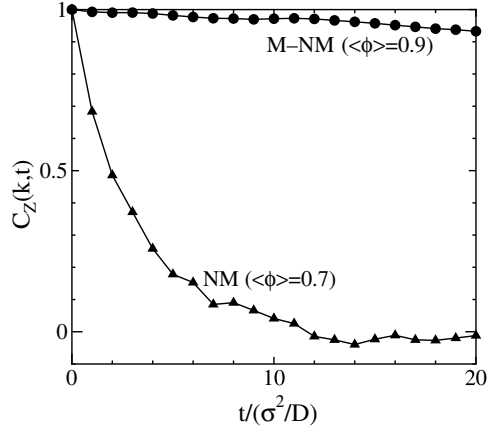
Figure 9. Relaxations of $C_Z(k, t)$ for $k\sigma = 0.245$ and $T = 1750$ K, where $C_{\text{grad}}/\sigma^2 = 1.0$ is adopted. Triangles and circles represent the simulation results for $\langle\phi\rangle = 0.7$ and 0.9, respectively; the full curves are for guides to the eyes.

related to the M–NM transition is the local ionization degree Z defined by equation (30). We thus consider the dynamical correlation function

$$C_Z(k, t) = \frac{\langle\delta Z(\mathbf{k}, t)\delta Z(-\mathbf{k}, 0)\rangle}{\langle\delta Z(\mathbf{k}, 0)\delta Z(-\mathbf{k}, 0)\rangle}, \tag{40}$$

with

$$\delta Z(\mathbf{k}, t) = \int_{L^2} d\mathbf{r}\, [Z(\mathbf{r}, t) - \langle Z\rangle] \exp(-i\mathbf{k} \cdot \mathbf{r}) \tag{41}$$

being the Fourier transform of $Z(\mathbf{r}, t)$. The simulation results for $C_Z(k, t)$ are displayed in figure 9. Slow relaxation is again observed for $\langle\phi\rangle = 0.9$; moreover, it is noteworthy that fast relaxation near $t \approx 0$ observed in $C(k, t)$ does not emerge in $C_Z(k, t)$. It can thus be concluded that the fast relaxation of $C(k, t)$ in the early stage corresponds to density relaxation
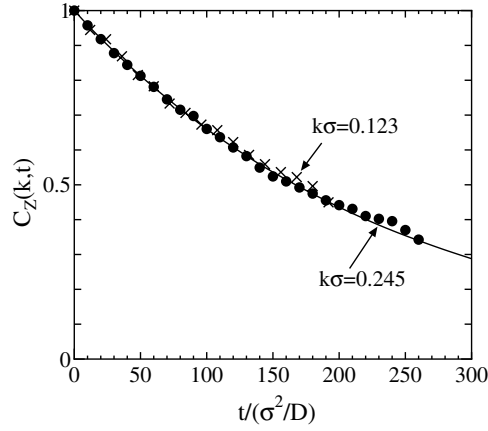
Figure 10. Long-time behaviour of $C_Z(k,t)$ for $k\sigma = 0.245$ (dots) and $k\sigma = 0.123$ (crosses) calculated at $\langle\phi\rangle = 0.9$ and $T = 1750$ K; $C_{grad}/\sigma^2 = 1.0$ is adopted. The full curve represents the exponential fit with $\tau = 241\sigma^2/D$.

without the M–NM transition, while the slow relaxation of $C(k,t)$ in the later stage originates from the transformation between metallic and nonmetallic domains. The former process is characterized by the conserved order parameter ϕ, while the non-conserved order parameter Z plays an essential role in the latter process.

In the nonmetallic phase ($\langle\phi\rangle = 0.7$), $C_Z(k,t)$ is related to the fluctuation of the 6p conduction electron densities, which originates from fluctuations of the local energy gap; time evolution of $C_Z(k,t)$ resembles that of $C(k,t)$ and does not exhibit slow relaxation, as figure 9 indicates. In the pure metallic phase, we have a trivial result $C_Z(k,t) = 1$ because $Z(\mathbf{r},t) = 2$ for any $\mathbf{r}$ and t.

We have also performed long-time simulations to observe time evolutions of $C_Z(k,t)$ at $\langle\phi\rangle = 0.9$ up to $t = 260\sigma^2/D$. As exhibited in figure 10, the result can be well reproduced by an exponential function, $C_Z(k,t) = \exp(-t/\tau)$, through which the relaxation time τ is obtained as $\tau = 241\sigma^2/D$ for $k\sigma = 0.245$. Noting that the diffusion constant of fluid mercury in the M–NM transition range may be estimated as $D \approx 2 \times 10^{-5}$ cm^2 s^{-1} by applying the Stokes' law [14], $D = k_B T/2\pi\eta\sigma$, to the measured shear viscosity η [38], we obtain $\tau \approx 9$ ns; this is roughly comparable to the experimental value of 2 ns [12]. When $C_{grad}/\sigma^2 = 9.0$ is adopted, the relaxation time becomes $\tau = 217\sigma^2/D$; the dependence of τ on C_{grad} is thus found to be fairly small. The relaxation time for $k\sigma = 0.123$ turns out to be close to that for $k\sigma = 0.245$.

6.3. Dependence on Δr

For all the cases in the present simulations, we have adopted $\Delta r = 4\sigma$, which corresponds to the estimated minimum mesh size [32] for which the use of bulk free energies may be valid. For comparison, we have also performed simulations with different values of Δr. Figure 11 illustrates the histograms of ϕ at $\langle\phi\rangle = 0.9$ obtained with $\Delta r/\sigma = 3, 4$ and 5. Density fluctuations tend to be enhanced as the degree of coarse-graining is reduced. When $\Delta r/\sigma = 3.0$, the value of the distribution function at $\phi = \phi_{MNM}$ is the largest among the three cases, which implies that the transformations between metallic and nonmetallic states occur most frequently; the corresponding relaxation time is found to be smaller by an order of magnitude than the case with $\Delta r/\sigma = 4.0$.
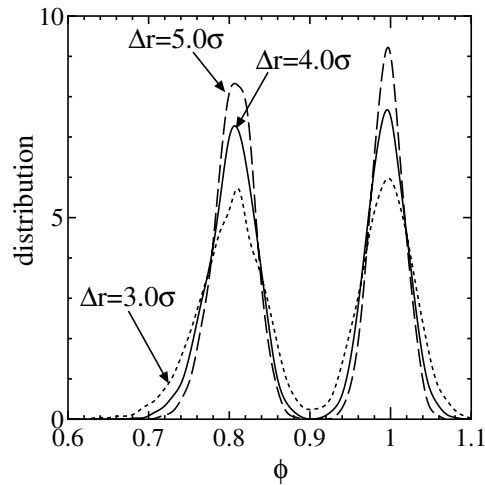
Figure 11. Histogram of ϕ at $\langle\phi\rangle = 0.9$ and $T = 1750$ K, obtained with $\Delta r/\sigma = 3.0$ (dotted curve), 4.0 (full curve) and 5.0 (broken curve); $C_{\mathrm{grad}}/\sigma^2 = 1.0$ is adopted.

If the domains were of macroscopic dimensions, convergent results would be obtained by choosing Δr as sufficiently smaller than the domain size yet substantially larger than the atomic size. Creation of macroscopic domains is expected near gas–liquid transitions [31], where $(\partial\mathcal{P}_{\mathrm{homo}}(\langle\phi\rangle)/\partial\phi)_T$ becomes extremely small and the gradient free energy makes a dominant contribution to the total free energy functional, equation (33). In the M–NM transition of mercury, however, a dominant contribution to the integrand on the right-hand side of equation (33) comes from the $(\partial\mathcal{P}_{\mathrm{homo}}(\langle\phi\rangle)/\partial\phi)_T$-related term rather than the C_{grad}-related term; the resultant phase patterns exhibit rather fine structures, as we have seen in figure 5.

Application of coarse-grained theories to such mesoscopic inhomogeneities would be the reason why the final results depend on Δr. Nevertheless, the advantage of our coarse-grained approach should be stressed, because this is the first theoretical demonstration of slow relaxation in the M–NM transitions of fluids, which has never been achieved by any microscopic approach.

7. Summary and discussion

In conclusion, we have proposed a new theoretical approach to the M–NM transitions in fluid mercury. Our theory is based on the dynamical LD equations for coarse-grained atomic densities, combined with the free energy formulae for bulk nonmetallic and metallic phases with the gradient correction.

Two important physical ingredients are involved in this formalism:

 (i) input bulk free energy showing the characteristics of an electron-induced first-order phase transition;
 (ii) Langevin force responsible for thermal fluctuations and structural disorder.

The former acts to enhance the *discontinuous* character of the M–NM transition, while the latter tends to smear out the discontinuities and to make the transition *continuous*. The overall picture of the M–NM transition may be determined through an interplay between these two competing effects. For instance, band overlap M–NM transitions in crystalline solids are

usually discontinuous [1, 2], because the latter effect does not play a role in the presence of a crystalline order. The present simulations indicate that *both* effects are crucial in the case of fluid mercury.

The basic characteristics of the M–NM transitions in fluid mercury obtained in this work are summarized: At low densities, the system is nonmetallic everywhere. As the average density increases, the local density can exceed ϕ_{MNM} by thermal fluctuation and metallic domains thus start to be created. In the M–NM transition range, metallic and nonmetallic domains, with the respective average densities of ϕ_{M} and ϕ_{NM}, are inhomogeneously mixed. Thermal fluctuations induce a local M–NM transition through transformation between the metallic and nonmetallic domains. The resultant pressure–density relation shows *continuous* behaviour across the M–NM transition. Isothermal compressibilities are significantly enhanced across the transition, but this leads to only a modest enhancement of the long-wavelength static structure factors, *not* in contradiction with the results of *ab initio* simulations [5] or x-ray diffraction measurements [9, 35]. Also, Cohen and Jortner [7] showed that such inhomogeneous domain structures can give a consistent explanation to the observed *continuous* change of transport coefficients in the M–NM transition.

The timescale of structural relaxation involving such a local M–NM transition is remarkably slow, because metallic and nonmetallic domains are highly stable and the transition between them is a rare event; this is a direct consequence of the input free energy exhibiting the nature of a first-order phase transition, as shown in figure 2. The experimentally deduced relaxation time of the order of nanoseconds [12] is consistent with our simulation results, with a characteristic domain size being approximately 4σ ($=11.6$ Å). This is roughly comparable to the estimation by Cohen and Jortner [7] based on the data of transport coefficients, which amounts to 30 Å.

In many cases, mechanisms of slow relaxation responsible for anomalous sound attenuation can be interpreted within a phenomenological two-state model, where the transition between a particular pair of states is regarded as a source of slow relaxation [39]. The appearance of distinct 'two states' (i.e. metallic and nonmetallic domains) manifested in figure 4 is quite reasonable in light of such a general relaxation theory.

The present theory starts from free energy models having the characteristics of a discontinuous phase transition as shown in figure 2, but this underlying discontinuity is relatively small. The predicted domain size and the density difference between the two phases are fairly small so that thermal fluctuations can significantly affect the nature of the transition; the final simulation results thus exhibit *continuous* M–NM transitions. The situation is in contrast to the gas–liquid phase separation, in which the domains have macroscopic dimensions, with substantial differences in the densities of the two phases. Such strongly discontinuous transitions are virtually unaffected by thermal fluctuations. We also note here that the non-ideal-plasma theory of Redmer *et al* [6] fails to reproduce the continuous M–NM transitions because the plasma theories treat the system as *homogeneous*. This fact again indicates the importance of the fluctuation effects on the M–NM transitions.

The results presented here are still insufficient for quantitative comparisons with experiments to be discussed, because we have adopted two-dimensional simulations and used crude models for the equations of state. The difference between two- and three-dimensional simulations may affect the amplitude of density fluctuations and hence the relaxation time. The probability distribution function $p(\phi)$ of local density fluctuations sampled for each discretized cell may be written as

$$p(\phi) \propto \exp\left\{-\frac{1}{2\langle\phi\rangle}\left(\frac{\Delta r}{\sigma}\right)^3\left(\frac{\partial \mathcal{P}_{\mathrm{homo}}(\langle\phi\rangle)}{\partial\phi}\right)_T(\phi-\langle\phi\rangle)^2\right\}, \tag{42}$$

which is an approximate expression in the sense that density fluctuations in every cell are assumed to be statistically independent with each other. Since the Δr-dependent factor in the exponent is $(\Delta r/\sigma)^3$ in the three-dimensional case, in contrast to $(\Delta r/\sigma)^2$ in the two-dimensional case, the amplitude of density fluctuations tends to be suppressed compared with the two-dimensional case studied here. On the other hand, the value of $(\partial \mathcal{P}_{\text{homo}}(\langle \phi \rangle)/\partial \phi)_T$ in the *true* M–NM transition range should be smaller than the present estimations, because the M–NM transition densities are significantly overestimated in this work. Smaller $(\partial \mathcal{P}_{\text{homo}}(\langle \phi \rangle)/\partial \phi)_T$ means a larger amplitude of density fluctuations. In order for correct predictions of the M–NM transition densities to be made, strong electron–ion interactions beyond the nearly-free electron model should be taken into consideration in the metallic equation of state.

Finally, we note that slow dynamics due to M–NM transitions has also been observed experimentally in Te_{50}–Se_{50} mixed fluids [41]. Mapping of the bulk free energy curve onto a simplified Ginzburg–Landau-type functional form [31, 40] would be helpful for a systematic study of various liquids, through which we might see whether slow dynamics due to M–NM transitions is a universal phenomenon.

Acknowledgments

Appendix. Derivation of equation (17)

The general expression for the band structure energy is given by [22, 23]

$$u_{\text{BS}} = \frac{1}{2k_{\text{B}}TV} \sum_{\mathbf{k} \neq 0} \frac{k^2}{4\pi e^2} \left[\frac{1}{\epsilon_{\text{e}}(k)} - 1 \right] |V^{\text{p}}(k)|^2 S(k). \tag{A.1}$$

Here, $\epsilon_{\text{e}}(k)$ refers to the static dielectric function of the electrons, $S(k)$ denotes the static structure factor of the ions and

$$V^{\text{p}}(k) = -\frac{4\pi Ze^2}{k^2} \frac{\sin(kR_{\text{M}})}{kR_{\text{M}}} \tag{A.2}$$

stands for the Fourier transform of the Shaw potential, equation (15).

To achieve the simplification of equation (A.1), the static dielectric function of the electron liquid may be approximated as

$$\epsilon_{\text{e}}(k) = 1 + \frac{1}{k^2 D_{\text{s}}^2}, \tag{A.3}$$

where D_{s} is given by equation (18). Furthermore, we replace $S(k)$ by that of a classical OCP and adopt a simple functional form:

$$S(k) = \frac{k^2}{k^2 + k_{\text{IS}}^2}, \tag{A.4}$$

where the parameter k_{IS} may be chosen so as to satisfy the thermodynamic consistency condition for OCP [42], namely

$$u_{\text{ex}}^{\text{OCP}} = \frac{1}{2k_{\text{B}}TV} \sum_{\mathbf{k} \neq 0} \frac{4\pi (Ze)^2}{k^2} [S(k) - 1]. \tag{A.5}$$

By substituting equation (A.4) into (A.5) and noting that $u_{\text{ex}}^{\text{OCP}} \approx -0.9\Gamma$ for $\Gamma > 1$ [42], we obtain $k_{\text{IS}} = 1.8/(Z^{1/3}a_{\text{e}})$. Then, equation (17) follows from equation (A.1).

References

[1] Hensel F and Warren W W Jr 1999 *Fluid Metals* (Princeton, NJ: Princeton University Press) chapters 2 and 4
[2] Yonezawa F and Ogawa T 1982 *Prog. Theor. Phys.* **72** (Suppl.) 1
[3] Yao M and Endo H 1982 *J. Phys. Soc. Japan* **51** 966
[4] Yao M 1994 *Z. Phys. Chem.* **84** S73
[5] Kresse G and Hafner J 1997 *Phys. Rev.* B **55** 7539
[6] Nagel S, Röpke G, Redmer R and Hensel F 1994 *J. Phys.: Condens. Matter* **6** 2137
    Redmer R 1997 *Phys. Rep.* **282** 35
[7] Cohen M H and Jortner J 1974 *Phys. Rev.* A **10** 978
[8] Franz J R 1986 *Phys. Rev. Lett.* **57** 889
[9] Tamura K and Inui M 2001 *J. Phys.: Condens. Matter* **13** R337
[10] Nara S, Ogawa T and Matsubara T 1977 *Prog. Theor. Phys.* **57** 1474
    Nara S, Ogawa T and Matsubara T 1979 *Prog. Theor. Phys.* **61** 736
    Ogawa T, Nara S and Matsubara T 1982 *Prog. Theor. Phys.* **72** (Suppl.) 140
[11] Hernandez J P and Martin L W 1990 *J. Non-Cryst Solids* **117/118** 481
[12] Kohno H and Yao M 1999 *J. Phys.: Condens. Matter* **11** 5399
    Kohno H and Yao M 2001 *J. Phys.: Condens. Matter* **13** 10293
[13] Landau L D and Lifshitz E M 1959 *Fluid Mechanics* (Oxford: Pergamon) chapter VIII (transl. J B Sykes and W H Reid)
[14] Hansen J-P and McDonald I R 1990 *Theory of Simple Liquids* 2nd edn (San Diego, CA: Academic) chapter 11
[15] Lust L M, Valls O T and Dasgupta C 1993 *Phys. Rev.* E **48** 1787
[16] Munakata T 1996 *Aust. J. Phys.* **49** 25
[17] Sancho J M, Lacasta A M, Torrent M C, Garcia-Ojalvo J and Tejada J 1993 *Phys. Lett.* A **181** 335
[18] Epstein L F and Powers M D 1953 *J. Phys. Chem.* **57** 336
[19] Lekner J 1967 *Phys. Rev.* **158** 130
[20] Hernandez J P, Schrönherr G, Götzlaff W and Hensel F 1984 *J. Phys. C: Solid State Phys.* **17** 4421
    Hernandez J P 1985 *Phys. Rev.* A **31** 932
[21] See e.g., Allen C W 1997 *Astrophysical Quantities* 3rd edn (London: Athlone Press) section 16
[22] Shimoji M 1977 *Liquid Metals* (London: Academic)
[23] Ashcroft N W and Stroud D 1978 *Solid State Phys.* **33** 1
[24] Ichimaru S 1994 *Statistical Plasma Physics* vol 2 *Condensed Plasmas* (Reading, MA: Addison-Wesley) chapters 1–3
[25] Vosko S H, Wilk L and Nusair M 1980 *Can. J. Phys.* **58** 1200
[26] Ceperley D M and Alder B J 1980 *Phys. Rev. Lett.* **45** 566
[27] Evans R 1970 *J. Phys. C: Solid State Phys.* **2** S137
[28] Kitamura H and Ichimaru S 1998 *J. Phys. Soc. Japan* **67** 950
[29] Young D A and Ross M 1984 *Phys. Rev.* B **29** 682
[30] Kohno H and Yao M 2002 *J. Phys.: Condens. Matter* **14** L171
[31] Lifshitz E M and Pitaevskii L P 1980 *Statistical Physics* part 1, 3rd edn (Oxford: Pergamon) chapter 14 (transl. J B Sykes and M J Kearsley)
[32] Pastor G M and Bennemann K H 1994 *Clusters of Atoms and Molecules* ed H Haberland (Heidelberg: Springer) p 86
[33] Evans R 1979 *Adv. Phys.* **28** 143
[34] Evans R and Sluckin T J 1981 *J. Phys. C: Solid State Phys.* **14** 3137
[35] Tamura K and Hosokawa S 1993 *J. Non-Cryst. Solids* **156–158** 646
[36] Oxtoby D W and Haymet A D J 1982 *J. Chem. Phys.* **76** 6262
[37] Langer J S 1974 *Physica* **73** 61
[38] Tippelskirch H v, Franck E U and Hensel F 1975 *Ber. Bunsenges. Phys. Chem.* **79** 889
[39] Herzfeld K F and Litovitz T A 1959 *Absorption and Dispersion of Ultrasonic Waves* (New York: Academic) chapter II
[40] Gleiser M 1994 *Phys. Rev. Lett.* **73** 3495
[41] Yao M, Itokawa N, Kohno H, Kajihara Y and Hiejima Y 2000 *J. Phys.: Condens. Matter* **12** 7323
[42] Ichimaru S 1992 *Statistical Plasma Physics* vol 1 *Basic Principles* (Reading, MA: Addison-Wesley) chapter 1